Robotica: (2020) volume 38, pp. 940–956. © Cambridge University Press 2019
doi:10.1017/S0263574719001188

# Internal Model Control and Experimental Study of Ankle Rehabilitation Robot

Lan Wang, Ying Chang* and Haitao Zhu

*College of Mechanical and Electrical Engineering, Harbin Engineering University, Harbin 150001, Heilongjiang Province, PR China*
*E-mails: wanglan@hrbeu.edu.cn, 365373956@qq.com*

(Accepted June 24, 2019. First published online: July 29, 2019)

**SUMMARY**
In the present work, the ankle rehabilitation robot (ARR) dynamic model that implements a new series of connection control strategies is introduced. The dynamic models are presented in this regard. This model analyzes the robot LuGre friction model and the nonlinear disturbance model. To improve the ARR system's rapidity and robustness, a composite 2-degree of freedom (2-DOF) internal model control (IMC) controller is presented. The control performance of the compound 2-DOF IMC controller is simulated and analyzed in the present work. The simulation shows that the composite 2-DOF IMC controller has high following performance. For practical testing purposes, 1-DOF passive training and predetermined trajectory following have been completed for different swing amplitudes and frequencies. Moreover, the thrust and tension torque of the robotic dynamic and static loading characteristics are studied in active control mode. The experimental results show the effectiveness of passive training of the given trajectory and impedance training active control strategy. This paper gives the specific functions of ARR.

KEYWORDS: Ankle rehabilitation robot; IMC control; Impedance training; Nonlinearity; Dynamic model.

## 1. Introduction

The ankle joint plays a key role in human walking and running.[1–3] Any injuries to the ankle would seriously intimidate daily activities. In this case, the ankle rehabilitation robot (ARR) can assist patients in joint flexibility and muscle strength training. In an aging society, the development of such a device has started since the 20th century. A research group at the Rutgers University[4,5] developed the Mega-Ankle robot which is a 6-degree of freedom (6-DOF) parallel ARR based on two small Stewart platforms. This robot can simulate actions including walking on the road and climbing stairs. However, its movement does not fully apply to patient activity or passivity.[6] Zhang et al. proposed a new adaptive patient-cooperative control strategy for improving the effectiveness and safety of robot-assisted ankle rehabilitation. However, they did not study the active control strategy.[7] Xie and Jamwal studied the 3-DOF pneumatic soft parallel robot which has four sets of air-driven arms and cables. The robot changes the length of the cables to perform platform movement. Thereby it can achieve a series of ankle exercises. However, the development of the control system is complicated.[8] Furthermore, a 3-DOF wearable ARR has been developed by Roy et al. in the Massachusetts Institute of Technology. It has a very low intrinsic mechanical impedance and weighs <3.6 kg. The joint between the foot and calf has 3-DOF, which can achieve 25° dorsiflexion, 45° plantar flexion, 25° inversion or eversion movement, and 15° internal or external rotation. However, the control

* Corresponding author. E-mail: changying0426@163.com

https://doi.org/10.1017/S0263574719001188 Published online by Cambridge University Press

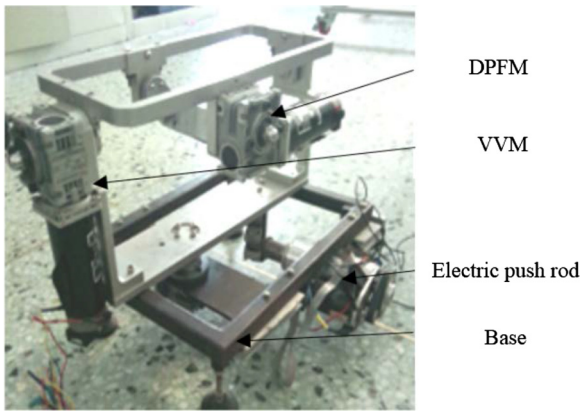



Fig. 1. ARR.

system did not realize the active recovery of ankle joint muscle function. Therefore, patients take little active participation in rehabilitation training.[9–11] Azcaray et al. proposed the generalized proportional integral (GPI) controller to guarantee safe rehabilitation movements. This parallel robot showed good results and various movement possibilities for lower limb rehabilitation. However, it is still in the simulation stage.[12] Bachir designed a kind of nonlinear IMC controller based on the Cartesian signal and applied the nonlinear IMC method to linearize high-power amplifier (PA) frequency in Bachir and Duvanaud. The results showed that the nonlinear IMC method can reduce the influence of nonlinearity and time delay.[13] Wen et al. investigated the IMC method in the position control loop, where the simulation results clearly demonstrated that the robustness of the IMC method outperforms other methods, such as the three-loop control method, the PI control method and the fuzzy-PID control method.[14] Zhou and Sagarakis presented a thorough kinematics analysis of a humanoid 2-DOF ankle module, based on a parallel kinematics mechanism. Therefore, patients take little active participation in rehabilitation training.[15] Based on simulation studies, Eilenberg et al. presented an adaptive muscle-reflex controller that utilizes an ankle plantar flexor comprising a Hill-type muscle with a positive force feedback reflex. They showed that the model's parameters are in a good agreement with the ankle's torque-angle profile.[16] Currently, there are two main kinds of ankle robots,[7] including wearable[17] and platform[18–20] robots. It should be indicated that platform robots are better suited for ankle exercises. However, the excessive cost and limited application potential are the major drawbacks of the state-of-the-art ARRs. It can be summarized from these literature review that further research is required to improve the two aspects. In a previous paper, the detailed structure of ARR has been studied.[21] The original contribution of the present work is to design a composite 2-DOF IMC controller for the ARR, which focuses on a specific control strategy. Dynamic models and simulation results are presented in this regard. It is intended to improve the ARR system's rapidity and robustness.

## 2. ARR

A prototype of the ARR is shown in Fig. 1.[21] Based on the UOT configuration, the 3-DOF turntable robot is designed, which is composed of the dorsiflexion-plantar flexion mechanism (DPFM), varus-valgus mechanism (VVM) and adduction-abduction mechanism (AAM). The robot can achieve 3-DOF of individual and compound movements. The robot's plantar flexion, dorsiflexion and varus-valgus mechanisms are driven by DC motors with worm gear reducers, which can realize the posture of a large space angle. The driving torque of the AAM is provided by the driving mechanism of the electric push rod and the connecting rod mechanism, which has the mechanical limiting function. The driving torque meets the requirements of the 3-DOF rehabilitation training for patients with ankle injury.

The control system of the ARR consists of a host PC and ARM controller. They communicate via the CAN bus. The host PC mainly completes the following functions: (1) setting movement parameters and rehabilitation modes; (2) displaying the current working state of the robot; (3) saving the rehabilitation training data; (4) protecting software security. On the other hand, the main functions of the ARM controller are as follows: (1) executing the host PC's control instruction; (2) driving

https://doi.org/10.1017/S0263574719001188 Published online by Cambridge University Press

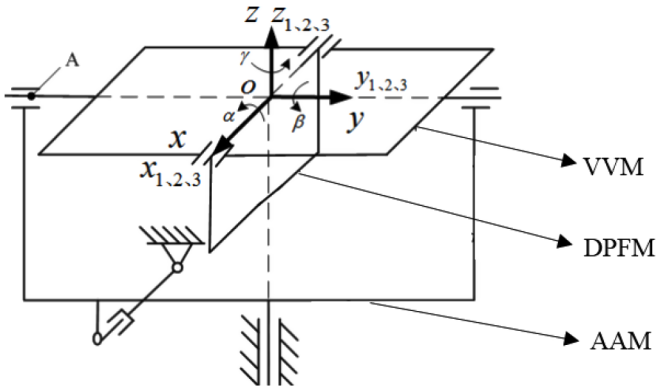



Fig. 2. Structural sketch and the coordinate system of the ARR.

the servo motor; (3) security protection. In order to facilitate the operation, the control system also includes an application for the smartphone, which is connected to the host PC through the Bluetooth.

## 3. Dynamic Model

Figure 2 illustrates the structural sketch and the coordinate system of the ARR. Initially, the institutional framework is in the horizontal state.

Figure 2 shows that $O_1 - x_1y_1z_1$, $O_2 - x_2y_2z_2$ and $O_3 - x_3y_3z_3$ are defined as the fixed coordinate systems of the DPFM, VVM and AAM, respectively. Moreover, it illustrates that the $x_1$ and $y_1$ axes are fixed with DPFM and VVM, respectively, while the $z_1$axis is fixed with the AAM and coincident with the inertial coordinate system $z_1$-axis.

Assuming that the three mechanisms mentioned above rotate around their fixed coordinate systems by $\alpha$, $\beta$ and $\gamma$ angles, respectively, the angular velocity of the mechanisms can be expressed as:

DPFM:

$$\begin{bmatrix} \omega_{1x} \\ \omega_{1y} \\ \omega_{1z} \end{bmatrix} = \begin{bmatrix} \dot{\alpha} \\ 0 \\ 0 \end{bmatrix} + T_\alpha \begin{bmatrix} 0 \\ \dot{\beta} \\ 0 \end{bmatrix} + T_{\alpha\beta} \begin{bmatrix} 0 \\ 0 \\ \dot{\gamma} \end{bmatrix} \tag{1}$$

VVM:

$$\begin{bmatrix} \omega_{2x} \\ \omega_{2y} \\ \omega_{2z} \end{bmatrix} = \begin{bmatrix} 0 \\ \dot{\beta} \\ 0 \end{bmatrix} + T_\beta \begin{bmatrix} 0 \\ 0 \\ \dot{\gamma} \end{bmatrix} \tag{2}$$

AAM:

$$\omega_{3z} = \dot{\gamma} \tag{3}$$

where

$$T_\alpha = \begin{bmatrix} 1 & 0 & 0 \\ 0 & \cos\alpha & \sin\alpha \\ 0 & -\sin\alpha & \cos\alpha \end{bmatrix}, \quad T_\beta = \begin{bmatrix} \cos\beta & 0 & -\sin\beta \\ 0 & 1 & 0 \\ \sin\beta & 0 & \cos\beta \end{bmatrix}, \quad T_{\alpha\beta} = T_\alpha T_\beta \tag{4}$$

where $\omega_{ij}$ denotes the angular velocity of the mechanism $i$ relative to the rotating axis $j$.

According to the dynamic equation of the rigid body rotating around the fixed point, the dynamic equations of each mechanism are obtained from the equations below:

$$\begin{cases} T_x = J_x \frac{d\omega_x}{dt} - (J_y - J_z)\omega_y\omega_z \\ T_y = J_y \frac{d\omega_y}{dt} - (J_z - J_x)\omega_z\omega_x \\ T_z = J_z \frac{d\omega_z}{dt} - (J_x - J_y)\omega_x\omega_y \end{cases} \tag{5}$$

https://doi.org/10.1017/S0263574719001188 Published online by Cambridge University Press

### *3.1. DPFM*

The torque acting on DPFM $\left(T_{1x}, T_{1y}, T_{1z}\right)^T$ can be obtained from Eq. (5). Furthermore, $T_{x-\text{internal}}$ is assumed to be a rotational torque which is loaded on the DPFM rotational axis $O-X_1$. Therefore, the kinetic equation can be written as:

$$\begin{aligned} T_{x-\text{internal}} = T_{1x} = &\left(J_{1z} - J_{1y}\right)\left(\dot{\gamma}\sin\alpha\cos\beta + \dot{\beta}\cos\alpha\right)\left(\dot{\gamma}\cos\alpha\cos\beta - \dot{\beta}\sin\alpha\right) \\ &+ J_{1x}\left(\ddot{\alpha} - \ddot{\gamma}\sin\beta - \dot{\gamma}\dot{\beta}\cos\beta\right) \end{aligned} \tag{6}$$

### *3.2. VVM*

$\left(T_{12x}, T_{12y}, T_{12z}\right)^T$ is assumed to be the torque that DPFM acts on VVM, which can be described as:

$$T_{12} = \left(T_{12x}, T_{12y}, T_{12z}\right)^T = \begin{bmatrix} 1 & 0 & 0 \\ 0 & \cos\alpha & -\sin\alpha \\ 0 & \sin\alpha & \cos\alpha \end{bmatrix} \begin{bmatrix} T_{1x} \\ T_{1y} \\ T_{1z} \end{bmatrix} \tag{7}$$

Moreover, $T_{y-\text{middle}}$ is assumed to be the torque loaded on the $O-Y_2$ axis and is the summation of the torques on the central axis of DPFM and the torques from VVM. Therefore, it can be written as:

$$T_{y-\text{middle}} = T_{2y} + T_{12y} \tag{8}$$

### *3.3. AAM*

The torque of AAM $\left(T_{3x}, T_{3y}, T_{3z}\right)^T$ can be obtained from Eq. (5). Assuming that the torques from DPFM and VVM are $\left(T_{13x}, T_{13y}, T_{13z}\right)^T$ and $\left(T_{23x}, T_{23y}, T_{23z}\right)^T$, respectively, then:

$$T_{23} = \left(T_{23x}, T_{23y}, T_{23z}\right)^T = \begin{bmatrix} \cos\beta & 0 & \sin\beta \\ 0 & 1 & 0 \\ -\sin\beta & 0 & \cos\beta \end{bmatrix} \begin{bmatrix} T_{2x} \\ T_{2y} \\ T_{2z} \end{bmatrix} \tag{9}$$

$$T_{13} = \left(T_{13x}, T_{13y}, T_{13z}\right)^T = \begin{bmatrix} \cos\beta & 0 & \sin\beta \\ 0 & 1 & 0 \\ -\sin\beta & 0 & \cos\beta \end{bmatrix} \begin{bmatrix} 1 & 0 & 0 \\ 0 & \cos\alpha & -\sin\alpha \\ 0 & \sin\alpha & \cos\alpha \end{bmatrix} \begin{bmatrix} T_{1x} \\ T_{1y} \\ T_{1z} \end{bmatrix} \tag{10}$$

$T_{z-\text{external}}$ is assumed to be the torque loaded on $O-Z_3$, and it is the sum of torques on DPFM, the VVM external torque projection on $O-Z_3$ and the applied torque on AAM. In other words, $T_{z-\text{external}}$ is written in the form below:

$$T_{z-\text{external}} = T_{3z} + T_{13z} + T_{23z} \tag{11}$$

After processing $T_1$, $T_2$ and $T_3$, the dynamic equations of these mechanisms are obtained as follows:

$$\begin{aligned} T_{x-\text{internal}} = &\ddot{a}J_{1x} - \ddot{\gamma}\ddot{\beta}\left[J_{1x}c\beta + \left(J_{1z} - J_{1y}\right)\left(c^2\alpha c\beta - s^2\alpha c\beta\right)\right] \\ &+ \ddot{\gamma}s\alpha c\alpha c^2\beta\left(J_{1z} - J_{1y}\right) + \ddot{\beta}^2\left(J_{1y} - J_{1z}\right)s\alpha c\alpha \end{aligned} \tag{12}$$

$$\begin{aligned} T_{y-\text{middle}} = &\ddot{\beta}J_{\text{middle}} - \ddot{\gamma}\left(J_{1y} - J_{1z}\right)s\alpha c\alpha c\beta + \dot{\gamma}^2\left(J_{2z} - J_{2x}\right)s\beta c\beta - J_{1x}s\beta c\beta \\ &+ \left(J_{1y}s^2\alpha + J_{1z}c^2\alpha\right) \times s\beta c\beta + \dot{\alpha}\dot{\beta}\left(2J_{1z} - 2J_{1y}\right)s\alpha \\ &+ \dot{\alpha}\dot{\gamma}\left[J_{1x}c\beta + \left(J_{1y} - J_{1z}\right)\left(c^2\alpha - s^2\alpha\right)c\beta\right] \end{aligned} \tag{13}$$

$$\begin{aligned} T_{z-\text{external}} = &\dot{\gamma}J_{z-\text{external}} - \dot{\alpha}J_{1x}s\beta + \beta\left(J_{1y} - J_{1z}\right)s\alpha c\alpha c\beta + \dot{\beta}\left(J_{1z} - J_{1y}\right)s\alpha c\alpha s\beta \\ &+ \dot{\beta}\dot{\gamma}\left[2J_{1x}\left(J_{1z} - J_{1y}\right)\left(s^2\alpha - c^2\alpha\right) - J_{1y} - J_{1z} + 2J_{2x} - 2J_{2z}\right]s\beta c\beta \\ &+ \dot{\alpha}\dot{\beta}\left[-J_{1x}c\beta + \left(J_{1y} - J_{1z}\right)\left(c^2\alpha - s^2\alpha\right)c\beta\right] + \dot{\alpha}\dot{\gamma}\left[2\left(J_{1y} - J_{1z}\right)\right]s\alpha c\alpha c^2\beta \end{aligned} \tag{14}$$

where

$$J_{y-\text{middle}} = J_{2y} + J_{1y}c^2\alpha + J_{1z}s^2\alpha \tag{15}$$

$$J_{z-\text{external}} = J_{3z} + J_{2x}s^2\beta + J_{2z}c^2\beta + J_{1x}s^2\beta + J_{1y}s^2\alpha\, c^2\beta + J_{1z}c^2\alpha\, c^2\beta \tag{16}$$

$$s\beta = \sin\beta,\ c\beta = \cos\beta,\ s\alpha = \sin\alpha,\ c\alpha = \cos\alpha.$$

https://doi.org/10.1017/S0263574719001188 Published online by Cambridge University Press

Table I. Rotational inertia (kgm$^2$).

| | | | | | |
|---|---|---|---|---|---|
| $J_{1x}$ | 4.37e–05 | $J_{2x}$ | 3.09e–04 | $J_{3x}$ | 0 |
| $J_{1y}$ | 2.79e–05 | $J_{2y}$ | 4.21e–03 | $J_{3y}$ | 0 |
| $J_{1z}$ | 3.23e–05 | $J_{2z}$ | 7.47e–04 | $J_{3z}$ | 5.32e–02 |

Equations (12)–(14) show that the rotational inertia and suffered torque of the three mechanisms are coupled. However, the ARR system actually works in the low speed state, where the angular velocity of each mechanism does not exceed 0.2 rad/s. Since the rotational inertia of the system is relatively small (see Table I), the influence of coupling effect is neglected in the present work.

## 4. Nonlinear Discussion Model

The nonlinear disturbance torque mainly includes friction, idle running and partial load torques. The friction torque will affect the process of starting and stopping of the system, especially in the low-speed stage. The friction torque leads to the crawling phenomenon of the system and affects system motion accuracy and stability. The idle running torque is generated by mechanical clearances and causes additional motion of components, accelerates the wear of mechanical parts and affects operational accuracy of the mechanical system. The existence of nonlinear partial load causes difference between the mechanism motion state before and after commutation. Therefore, the speed curve has a asymmetric pattern.

### *4.1. Mathematical model of friction torque* $\boldsymbol{T_f}$

In the present section, a simplified LuGre model is employed to describe the robot friction characteristics. The LuGre model describes the correlation between friction torque and rotational speed.[22–24] Moreover, it accurately describes the creep phenomenon and the Stribeck friction effect. The LuGre model applies the first-order differential equation to model friction force. Using the mane model, the Stribeck and the average change effects in the Dahl model are well described and the dynamic and static friction characteristics are analyzed. Since so many parameters of the model need to be determined, the simplified model is usually used[25,26] as shown in Eq. (17):

$$T_f = \text{sign}\,(\omega)\,T_c + \text{sign}\,(\omega)\,(T_s - T_c)\,e^{-(\omega/\omega_s)^2} + \delta_2\omega \tag{17}$$

where $T_f$, $T_s$and $T_c$ are the friction torque, the maximum static friction torque and the Coulomb friction torque, respectively. Moreover, $\omega$, $\omega_s$ and $\delta_2$ denote the relative angular velocity of the rotating mechanism, the stribeck angular velocity and the viscous friction coefficient, respectively.

The driving mode of VVM is the same as that for DPFM, so that there are partial load disturbances affecting the establishment of the friction model. The specific process of parameter determination is as follows:

1) Five sets of starting current and speed data are collected. The data are fitted by the fitting toolbox of MATLAB, called "cftool", to calculate the maximum average value of the starting current. Then the maximum static friction ($T_s$) is calculated.
2) Under the condition of uniform speed, the correlation between 10 groups with different speeds and currents is collected. Curve fitting is applied on 10 sets of velocity values and 10 sets of current values, employing the "cftool" fitting toolbox.
3) Considering the obtained velocity and current curves and the $T_s$ value from the experiment, Eq. (17) is employed to simulate the friction torque so that the parameters $T_c$, $\delta_2$ and $\omega_s$ can be calculated.

### *4.2. Idle running impact torque* $\boldsymbol{T_p}$ $\boldsymbol{(t)}$

A mathematical model of idle running has not been established yet, because its impact on the system is complex. Furthermore, it is too difficult to eliminate idle running by the control system for large clearances. In order to reduce the impact of idle running, the mechanical transmission systems except the AAM are preloaded. The worm gear reducer is replaced with a larger clearance one.

https://doi.org/10.1017/S0263574719001188 Published online by Cambridge University Press

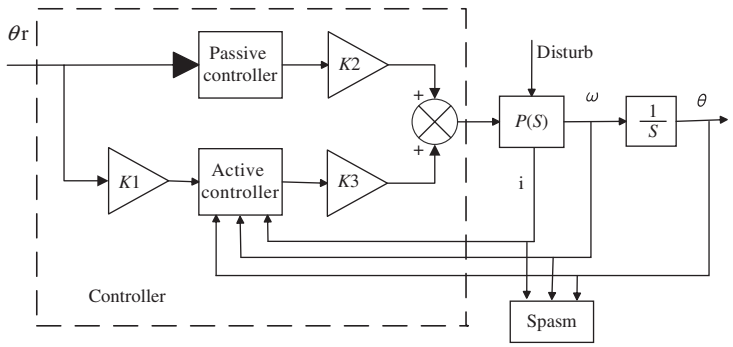



Fig. 3. Compound controller for the ankle joint rehabilitation robot.

### *4.3. Mathematical model of partial load torque* $\boldsymbol{T_d}$ $(\boldsymbol{\phi})$

The partial load torque is mainly caused by the VVM movement as expressed below:

$$T_d(\phi) = T_g r \sin(\phi) \tag{18}$$

where $r = 0.09$ m is the maximum arm of the partial load torque$r$; $T_g = G_m r$, where $T_g$ is the maximum torque generated by the drive motor gravity of DPFM. Moreover, $G_m = 10$ N denotes the partial load weight and $\phi$ is the rotational angle of VVM relative to the initial position. Its positive direction is in the counterclockwise along the negative direction of the $y$-axis.

In terms of the analytical results above, the nonlinear disturbance torque ($T_l(\phi, \omega)$) is stated as:

$$T_l(\phi, \omega) = T_d(\phi) + T_f \tag{19}$$

## 5. Control Strategy

ARR is mainly employed to restore the joint movement of functional training and improve the muscle strength of active training. Because of its simple tuning procedure and good set-point tracking capabilities, there have been some works in combining IMC to facilitate the processes mentioned above in the robotic mode.[27–30] Because of its simple structure and easy implementation, many machines have used IMC.[31,32] A composite controller based on the IMC passive control with 2-DOF and resistive active control is designed. In order to improve the reliability and stability of the motion control of ARR, the protection function of the control system includes patient's lower limb spasm and the overrunning signal in the rehabilitation training process, as shown in Fig. 3. The system input is the position signal ($\theta_r$). Furthermore, the passive training parameters are set to $k2 = 1$ and $k3 = 0$. A passive controller acts to achieve the movement trajectory control. Moreover, the active training parameters are set to $k2 = 0$ and $k3 = 1$. An active controller acts to $k1$ position signal into current reference to achieve current control. The robot position and the current output signal are used to determine whether the robot and patient movement is normal so that, in case of a robot failure or lower limb spasm, the controller is adjusted timely.

### *5.1. Passive controller*

The corresponding mathematic model of the nonlinear friction and nonlinear eccentric load disturbances have been established. Moreover, the characteristics of the feedforward-feedback controller have been analyzed above.

1) PD controller

The PD controller can be expressed as:

$$u_{pd}(s) = k_p + k_d Ns/(1+Ns) \tag{20}$$

where $k_p$ and $k_d$ are individually adjusted. Differential link has high-pass filters, and the turning frequency is equal to $N$.

https://doi.org/10.1017/S0263574719001188 Published online by Cambridge University Press

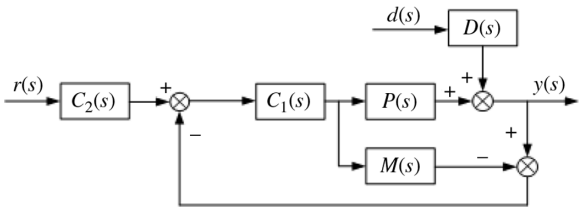



Fig. 4. Block diagram of the 2-DOF IMC controller.

2) 2-DOF IMC controller

The IMC controller with 2-DOF is used for position control. Two independent IMC controllers are used to adjust the system's rapidity and robustness. Moreover, the feedforward controller is increased so that the controller improves the following performance and anti-perturbation performance of the system, while accelerating the system response speed of nonlinear disturbance. Therefore, the steady-state error of the system reduces.

A block diagram of the IMC controller with 2-DOF is shown in Fig. 4, where $C_1\ (s)$, $C_2\ (s)$ and $P\ (s)$ are the stable IMC controller, the following IMC controller and the controlled object, respectively. Furthermore, $M\ (s)$, $r\ (s)$, $y\ (s)$ and $d\ (s)$ denote the internal model of the controlled object, the system input, the system output and the disturbance, respectively. The stable IMC controller is mainly used to adjust the robustness of the system and enhance the system's ability to resist disturbance. The following IMC controller is mainly used to adjust the system's following performance.

Figure 4 shows that

$$y\ (s) = \frac{C_1\ (s)\ C_2\ (s)\ P\ (s)}{1+\mathrm{C}_1\ (s)\ [P\ (s) - \mathrm{M}\ (s)]} r\ (s) + \frac{1 - M\ (s)\ C_1\ (s)\ D\ (s)}{1+\mathrm{C}_1\ (s)\ [P\ (s) - \mathrm{M}\ (s)]} d\ (s) \tag{21}$$

Considering $P\ (s) = M\ (s)$, Eq. (21) can be rewritten as:

$$y\ (s) = \mathrm{C}_1\ (s)\ C_2\ (s)\ M\ (s)\ r\ (s) + [1 - \mathrm{M}\ (s)\ C_1\ (s)]\ D\ (s)\ d\ (s) \tag{22}$$

In order to facilitate the design, the system internal model $M\ (s)$ is decomposed into $A\ (s)$ and $B\ (s)$, in the following way: $M\ (s) = A\ (s)\ B\ (s)$, where $A\ (s)$ is composed of the zero point of the right half plane of the controlled object and pure lag link, while $B\ (s)$ denotes the minimum phase system. Furthermore, $C_1\ (s)$ often uses the conventional design methods, as follows:

$$C_1\ (s) = B(s)^{-1} \frac{1}{(1 + \lambda_1 s)^{\mathrm{n}}} \tag{23}$$

On the other hand, $C_2\ (s)$ often uses the following form:

$$C_2\ (s) = \frac{(1 + \lambda_2 s)^m}{(1 + \lambda_1 s)^n} \tag{24}$$

The selection of $m$ and $n$ should make the system feasible. Their numerical value is determined according to the order of $B\ (s)$.

Applying Eqs. (22) and (23) into Eq. (21) yields:

$$y\ (s) = \frac{B(s)^{-1}}{(1+\lambda_1 s)^n} \frac{(1+\lambda_1 s)^n}{(1+\lambda_2 s)^m} M\ (s)\ r\ (s) + \left[1 - M\ (s)\ \frac{B(s)^{-1}}{(1+\lambda_1 s)^n}\right] D\ (s)\ d\ (s) \tag{25}$$

Equation (25) shows that the change of $\lambda_2$ can adjust the following performance, and the change of $\lambda_1$ can adjust the robustness of the system for the 2-DOF IMC.

Each controller of the 3-DOF robot has the same design methods. The model of VVM is studied as the controlled object. The parameters of the driving motor are listed in Table II. The parameters of the equivalent rotational inertia of the robot are illustrated in Table III. The transfer function of the rotational speed ($\omega$) and the input voltage ($u$) can be obtained from the following equation:

$$P(s) = \frac{1}{0.018s^2 + 0.36s + 0.05} \tag{26}$$

https://doi.org/10.1017/S0263574719001188 Published online by Cambridge University Press

Table II. DC motor parameters.

| **Motor model** | ***P*** | $T_N$ | $\omega N$ | $I_N$ | ***U*** |
|---|---|---|---|---|---|
| 50SYXBJ | 80 W | 0.4 Nm | 2000 rpm | 5 A | 24 V |
| $T_m$ | $L_a$ | $R_a$ | $B$ | $J$ | $C_m$ |
| 0.05 N.m/A | 0.0013 H | 2.6Ω | 2e–4 | 1.86e–5 kg.m$^2$ | 0.05 V.s/rad |

Table III. Equivalent moment of inertia parameters of the robot rotation mechanism (kgm$^2$).

| Rotation mechanism | DPFM | VVM | AAM |
|---|---|---|---|
| Equivalent moment of inertia | 4.37e–05 | 4.21e–3 | 3.39e–2 |

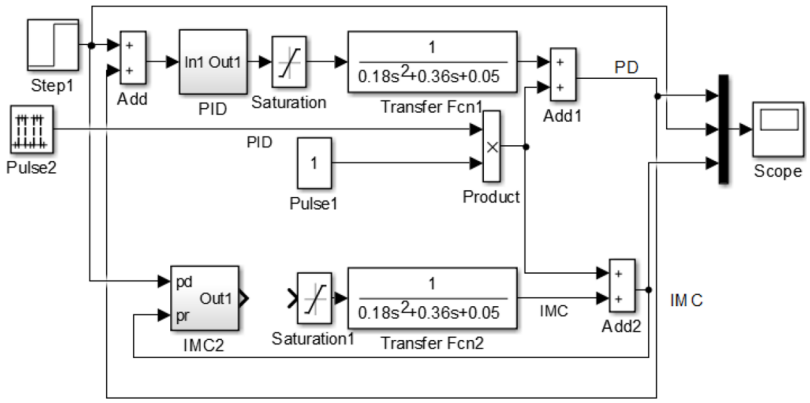



Fig. 5. Controller analysis and comparison program.

For Eq. (26), the poles are in the left half plane, and the system is stable. So $B(s) = P(s)$. In order for the system to have physical feasibility, the parameters in Eqs. (23) and 24 are set to $m = 2$ and $n = 2$, respectively. Then the controllers can be given as follows:

$$C_{21}(s) = \frac{0.18s^2 + 0.36s + 0.05}{(\lambda_1 s + 1)^2} \quad C_{22}(s) = \frac{(1 + \lambda_2 s)^2}{(1 + \lambda_1 s)^2} \tag{27}$$

### *5.2. Controller simulation analysis*

The control effect of 2-DOF IMC and PD controllers is mainly analyzed in this section. The simulation program diagram is shown in Fig. 5.

First of all, in the case of no disturbance signal, the same step signal is applied and the controller parameters are adjusted. Different amplitudes are set to observe the output response of the PD and the 2-DOF IMC controllers. Then, in order to analyze and compare the two kinds of controller's ability to restrain disturbance, the same amplitude of pulse disturbance is loaded at the same position.

Initially, the step amplitude is set to 1 rad. The PD controller parameters are set to $K_p = 53$, $K_d = 18$, while the 2-DOF IMC controller parameters are set to $\lambda_1 = 0.15$, $\lambda_2 = 0.25$. Then, the step amplitude is given to observe the system response. Finally, a pulse disturbance signal with an amplitude of 0.05 rad is added, as displayed in Fig. 6.

Figure 6(a) shows that when the amplitude of the step is large, the rise time of the 2-DOF IMC controller is faster compared to that for the PD controller. On the other hand, Fig. 6(b) illustrates that when the step amplitude is small, the rise time of the PD controller is faster than that for the 2-DOF IMC controller, but it has a poor steady-state accuracy. After adding disturbance, Fig. 6(c) shows that the 2-DOF IMC controller has better following performance, regardless of the amplitude. Moreover, the rapidity and anti-disturbance ability of the system increase. This system parameter is easy to adjust.

https://doi.org/10.1017/S0263574719001188 Published online by Cambridge University Press

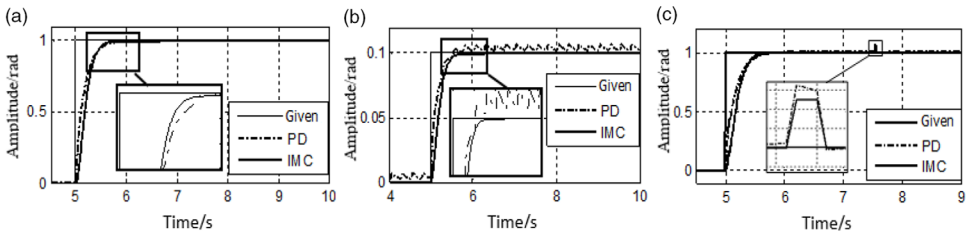



Fig. 6. Controller simulation analysis results.

### *5.3. Active controller*

The impedance training controller converts the collected deflection angle signal ($\psi$) to the upper computer through the Bluetooth and serial communication bus, and $I_d$ is the given signal of the upper computer current closed loop control. There is a linear correlation between deflection angle, signal and proportion coefficient $k_i$:

$$\psi = I_d k_i \tag{28}$$

The design of the active control algorithm for impedance training mainly includes two parts: (1) analysis and design of data smoothing and prediction algorithm; (2) analysis and design of impedance training control algorithm.

1) Data smoothing filter design

In order to improve the control performance of the system, it is necessary to filter the current signal. Meanwhile, in the process of using a smartphone to control the robot, the weak jitter of the hand causes significant changes in the mobile attitude (MA) signal in a moment. When the jitter amplitude is large enough, it seriously interferes with the normal operation of the robot. It should be indicated that the limit-weighted sliding average filtering method is used in the present work to smooth the received mobile attitude signal.

Assuming that the queue length is $N$, the queue array is buffer [$N$], the weighting factors are $C_0, C_1 \ldots\ldots C_{N-2}, C_{N-1}$ and the upper and lower limits are $A_u, A_d$, respectively. Then the output value satisfies:

$$\begin{cases} \text{buffer}[i] = A_u & \text{buffer}[i] >= A_u \\ \text{buffer}[i] = A_d & \text{buffer}[i] <= A_d \end{cases} \quad i = 0, 1, \ldots\ldots N-1 \tag{29}$$

The queue length of $N$ remains constant. The latest sampling data are judged by amplitude limiting, while the data exceeding the limit are replaced by amplitude limiting. The data fulfilling the judgment condition are put into the weighted sliding filter queue so that the queue satisfies the first-in first-out (FIFO) principle. Based on the rapid response of the system, the weighting factor is selected according to the actual situation to ensure that the new data can be reflected in real time.

2) Design of impedance training controller

The impedance training controller is designed based on the feedforward and the current closed-loop controls. Equation (30) is the correlation between friction torque compensation current ($I_f$) and friction torque:

$$I_f = \frac{\left( \text{sgn}\,(\omega)\, T_c + \text{sgn}\,(\omega)\,(T_s - T_c) \left( 1 + \left( \frac{\omega}{\omega_s} \right) + \frac{\left( \frac{\omega}{\omega_s} \right)^2}{2} \right) + \delta_2 \omega \right)}{T_m} \tag{30}$$

where $T_m$ is a constant denoting the motor torque. Equation (18) shows that the current compensation of the partial load torque is given by:

$$I_g\,(\phi) = \frac{T_g r \sin\,(\phi)}{T_m} \tag{31}$$

https://doi.org/10.1017/S0263574719001188 Published online by Cambridge University Press

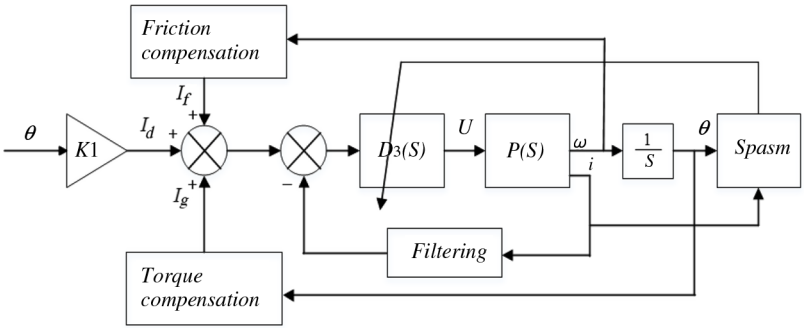



Fig. 7. Compound PI controller.

The impedance training controller uses the feedforward and the current closed-loop controller as shown in Fig. 7. Because of the limitation of the experimental environment, the friction compensation is considered in the controller design process. The friction compensation is the friction torque compensation function, and the output is the compensation current. The function relations can be found by Eq. (30). The torque compensation is a partial load torque compensation function, and its output is the compensation current, which is shown in Eq. (31). These two compensation current values are superimposed with the given current $I_d$ as the actual given for the current closed loop. $D_3$ $(s)$ is the PI controller. It is expressed as $u_{pi}$ $(s) = k_p + u_i$ $(s)$. The closed-loop current control is realized. The integral link $u_i$ $(s) = k_i/s$ contains clipping and clearing and eliminates the phenomenon of output transitions due to the presence of the integral value in the switched state.

## 6. Experiments and Results

The hardware and software are analyzed by experiments to verify the theoretical results. Moreover, the LuGre model parameters and the improved mechanical structure are analyzed and verified. In this section, 1-DOF predetermined path passive control experiment, 1-DOF and 2-DOF autonomous trajectory passive training control experiments are performed under load condition. As a result, a theoretically predicted function is experimentally analyzed and summarized.

### *6.1. Passive training experiment of the given trajectory*

In order to analyze the passive training performance of the robot, the data are collected under load. The weight and height of the experimenter are 65 kg and 175 cm, respectively. The feedforward controller friction model parameters and the IMC controller parameters are as follows:

Parameters for DPFM: $\lambda_1 = 0.17$, $\lambda_2 = 0.2$.
Parameters for VVM: $\lambda_1 = 0.15$, $\lambda_2 = 0.25$.
Parameters for AAM:$\lambda_1 = 0.09$, $\lambda_2 = 0.23$.

1) 1-DOF passive training experiment

The corresponding parameters of the 1-DOF passive training are set before the experiment. The sinusoidal trajectory signal amplitudes of DPFM are set to 0.087, 0.174 and 0.348 rad, respectively. The frequencies are set to 0.5, 0.1 and 0.05 Hz. The sinusoidal trajectory signal amplitudes of VVM are set to 0.087, 0.174 and 0.348 rad, respectively. Moreover, the frequencies are set to 0.5, 0.1 and 0.05 Hz. The sinusoidal trajectory signal amplitudes of AAM are set to 0.087, 0.174 and 0.348 rad, respectively. Furthermore, the frequencies are set to 0.5, 0.1 and 0.05 Hz. Figures 8–10 show the position tracking error curve of the robot in the presence of different swing amplitudes and frequencies under load. It should be indicated that subfigures(a)–(c) correspond to DPFM, VVM and AAM, respectively.

Figures 8–10 illustrate that the maximum error of the 1-DOF passive trajectory tracking is 0.021 rad, and the robot operation error is small. It is observed the steady-state error of the system remains small as swing amplitude increases. Furthermore, the system following error increases from 1.3% to 5.4% as the swing frequency increases. The main reason is that when the frequency is too fast, the influence of model uncertainty on the accuracy of the system increases.

https://doi.org/10.1017/S0263574719001188 Published online by Cambridge University Press

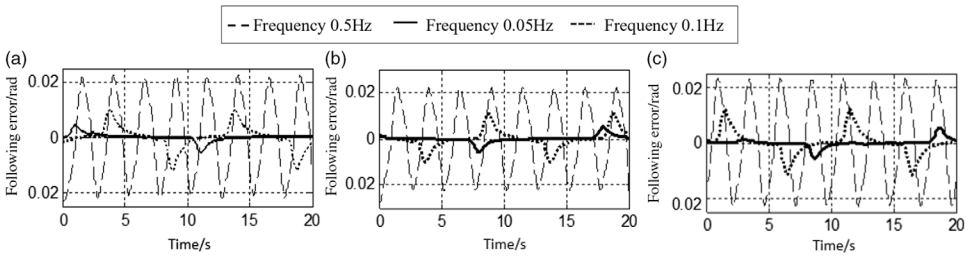



Fig. 8. Passive training curve with an amplitude of 0.087 rad.

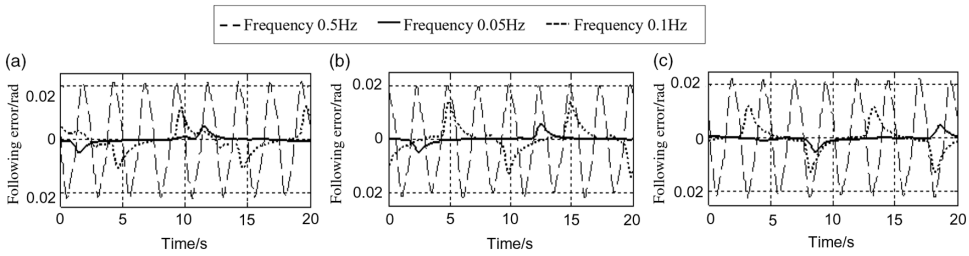



Fig. 9. Passive training curve with an amplitude of 0.174 rad.

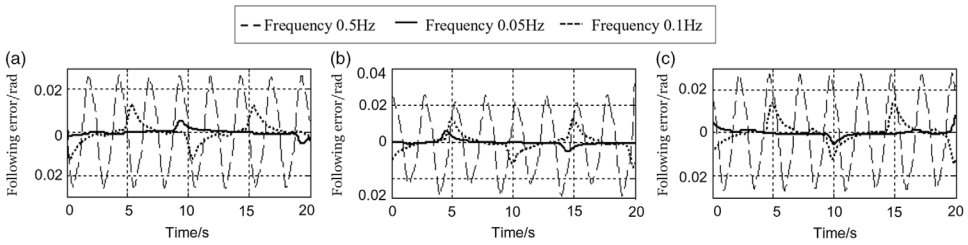



Fig. 10. Passive training curve with an amplitude of 0.384 rad.

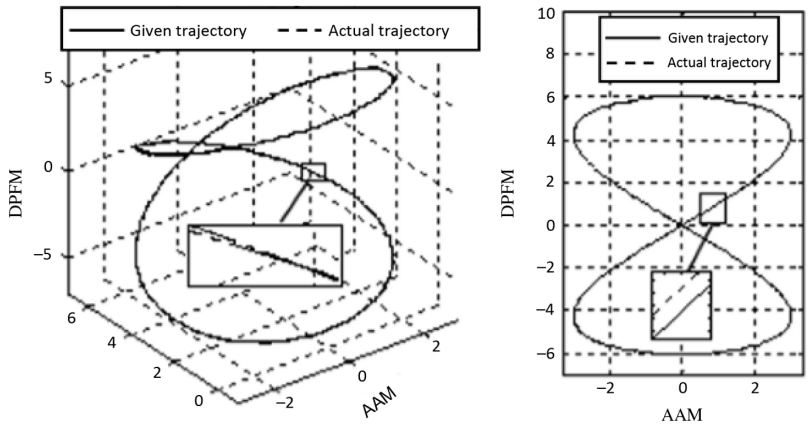



Fig. 11. Following curve of predetermined trajectory.

2) Predetermined trajectory experiment

The predetermined trajectory is measured according to the set of toe movement trajectory. The training trajectory of each joint of the ankle joint rehabilitation robot is calculated based on toe movement. Figure 11 indicates that the experiment is carried out in the case of load, given the position curve of the two joint rotations. It can be seen from the curve that the mechanism is stable and the tracking error of the moving mechanism is basically the same as that for the individual

https://doi.org/10.1017/S0263574719001188 Published online by Cambridge University Press

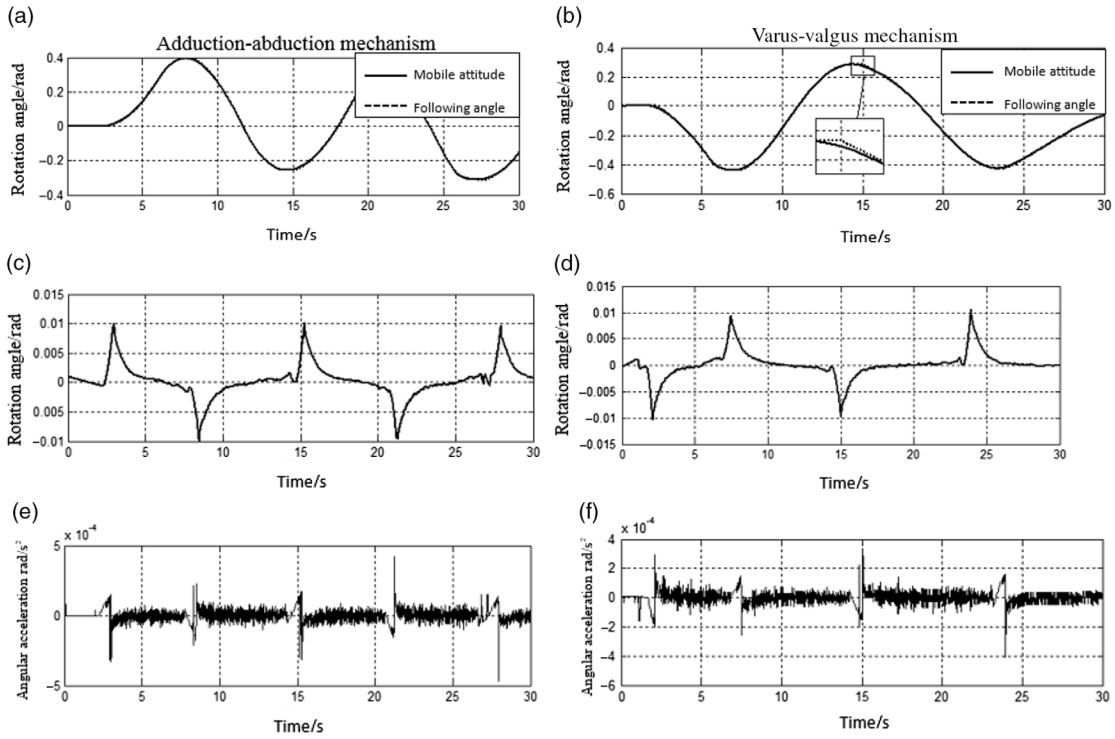



Fig. 12. 1-DOF position active control experiment curves: (a) DPFM position following curve. (b) VVM position following curve. (c) DPFM position following error curve. (d) VVM position following error curve. (e) DPFM active control angular acceleration curve. (f) VVM active control angular acceleration curve.

running position. The experimental results show that the coupling effect of the turntable in the low speed state has no obvious effect on system operation and the robot can achieve the predetermined trajectory training and stable operation.

3) 1-DOF autonomous trajectory passive training experiment

The main contents of the study include the position training control of DPFM and VVM. In the position training control experiment, the compound 2-DOF IMC controller parameters are consistent with the ones in the passive training control experiment. Moreover, the impedance training active control feedforward controller parameters are consistent with the parameters of the passive feedforward controller. The parameters of the PI controller are set as follows:

Parameters for DPFM: $k_p = 7$, $k_i = 32$, $k = 8$.

Parameters for VVM: $k_p = 9$, $k_i = 35$, $k = 8$.

Before the autonomous trajectory passive motion experiment of DPFM, the three rotating mechanisms are in the initial state. The results of the robot's active control follow-up experiment curves are shown in Fig. 12(a)–(f).

The experimental curves indicate that the position following error is kept within 0.01 rad and the angular acceleration is less than the sensory threshold ($2.1 \times 10^{-3}$rad/s$^2$) of human body diagonal acceleration. It can be concluded that when the patient is active in 1-DOF position control, the body does not perceive the jitter of the robot.

4) 2-DOF autonomous trajectory passive training experiment

DPFM and VVM are selected to perform the 2-DOF autonomous trajectory passive control. Before starting the training, the mechanism is set up in accordance with the exercise requirements. When carrying out 2-DOF autonomous trajectory passive control, we need to select two mechanisms and passive motion mode at the same time, set the sensitivity to be moderate, then click the start

https://doi.org/10.1017/S0263574719001188 Published online by Cambridge University Press

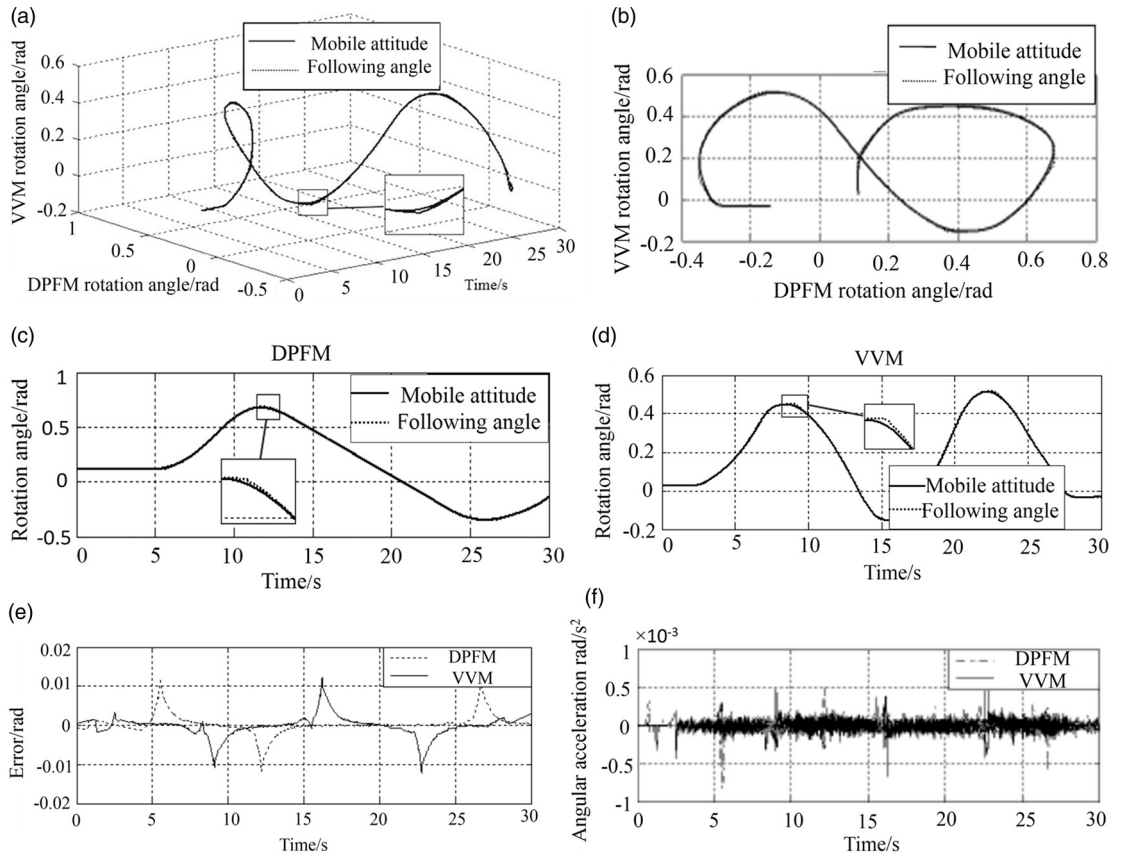



Fig. 13. 2-DOF autonomous trajectory passive control experiment curves: (a) Spatial trajectory curve. (b) *O*xyplane projection traject. (c) DPFM position following curve. (d) VVM position following curve. (e) Position error curve. (f) Angular acceleration curve.

button to train. Figure 13(a)–(f) illustrates the results obtained from the experiment for the 2-DOF autonomous trajectory passive control.

### *6.2. Impedance training active control experiment*

A 1-DOF impedance active control is mainly used for DPFM and VVM. It should be indicated that only one mechanism is allowed to exercise resistance active control at a time. The experiment mainly includes two parts: (1) static loading thrust and tension, (2) dynamic loading thrust and tension. The right foot is supposed to be the experimental body. The thrust and tension provided by DPFM depend on the force of the forefoot, while the thrust and tension force provided by VVM is evaluated by the force on the medial foot.

The active control of static loading is mainly used for the exercise of ankle joint tendon in the early stage of muscle recovery, while the dynamic loading active control is mainly used in the late recovery of ankle joint to provide a greater external force so that the peroneal muscle, soleus muscle, tibialis anterior muscle and varus muscle can get a better exercise.

1) Static loading experiment

The length of the limiting amplitude-weighted sliding filter is set to 10 in the experiment. Moreover, the weighted coefficients are 0.01, 0.03, 0.05, 0.07, 0.09, 0.11, 0.13, 0.15 and 0.19. The experimental current curve and current error curve of the DPFM static thrust and tension loading are presented in Figs. 14 and 15, respectively.

The current curve and current error curve of the VVM static thrust and tension loading are presented in Figs. 16 and 17, respectively.

https://doi.org/10.1017/S0263574719001188 Published online by Cambridge University Press

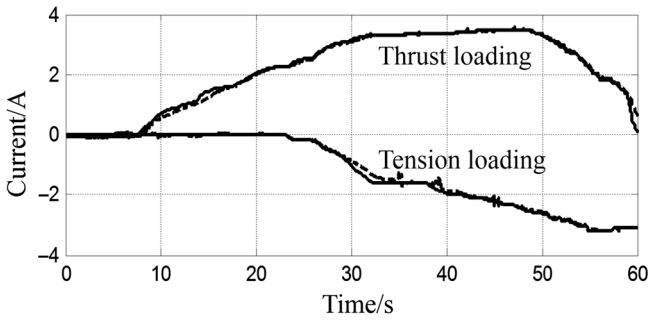



Fig. 14. Load current curve of thrust and tension.

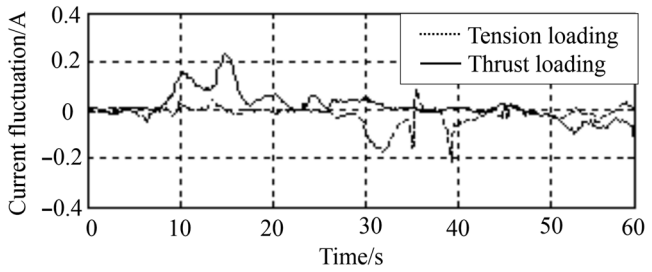



Fig. 15. Load current error curve of thrust and tension.

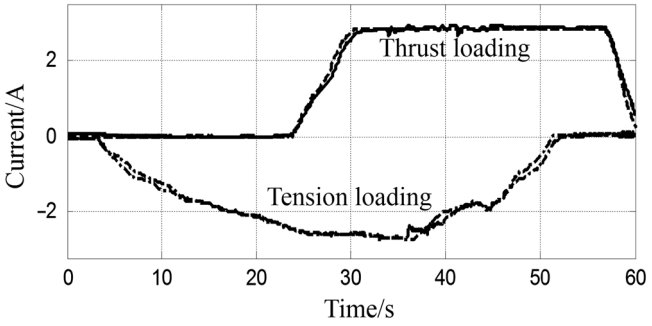



Fig. 16. Load current curve of thrust and tension.

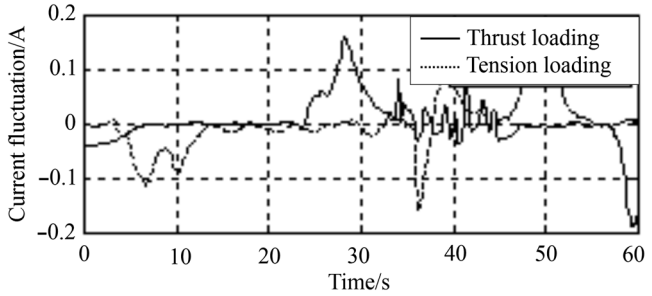



Fig. 17. Load current error curve of thrust and tension.

During the experiment, it was observed that the motor torque increases as load current increases. The current curve also changes when the footsteps are jittering. The maximum error of the experimental current of VVM is 0.15 A. The change rate of the torque applied to the foot is small and the robot runs smoothly.

https://doi.org/10.1017/S0263574719001188 Published online by Cambridge University Press

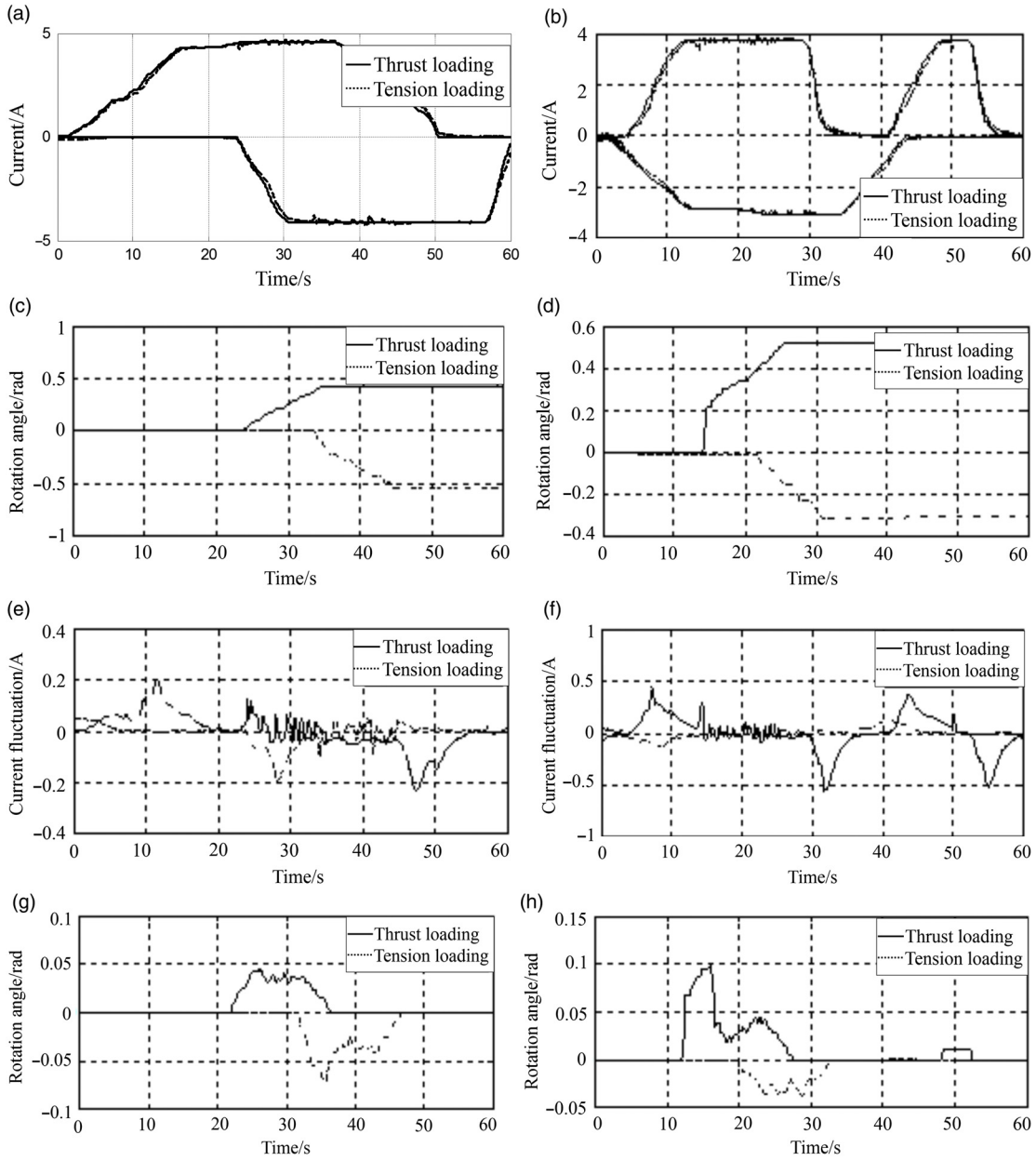



Fig. 18. Dynamic loading curves of thrust and tension. (a) Load current curve of DPFM. (b) Load current curve of VVM. (c) Load position curve of DPFM. (d) Load position curve of VVM. (e) Load current error curve of DPFM. (f) Load current error curve of VVM. (g) Load speed curve of DPFM. (h) Load speed curve of VVM.

2) Dynamic loading experiment

In the process of dynamic loading, the smoothing filter parameters are consistent with the ones for static loading. During the experiment, the robot exerts a dynamic force on the foot. At the same time, the experimental personnel change the force of the foot reaction to the robot. Figure 18(a)–(h) shows the dynamic thrust and tension load curves of DPFM and VVM.

It is observed from the experimental results that the motor torque increases as load current increases. On the other hand, when the footstep force is jittering, the current curve changes with the external force and the robot can complete the load of the torque quickly and stably.

The experimental results show that the position following error is within 0.012 rad. The angular acceleration is less than the sensory threshold of diagonal acceleration. The robot can move according to the expectation of the experimenter. Moreover, the robot can run quickly and steadily.

https://doi.org/10.1017/S0263574719001188 Published online by Cambridge University Press

The experiments have been conducted to validate the performance of hardware and software. Furthermore, the experimental results prove that the ARR achieves the purpose of the project. The passive training experiment of the ARR for different amplitudes shows that the trajectory following error of the robot is basically kept within 0.012 rad. The commutation process and the low speed process are the most influential time of nonlinear disturbance. It can be seen from the experimental curve that the angular velocity of the three rotating mechanisms of the robot is relatively gentle during the commutation process, and there is no obvious peak in the angular acceleration curve. Moreover, there is no crawling phenomenon, which indicates that the control system plays a significant inhibitory effect on nonlinear disturbances.

Through the human–machine experiments, it was found that the variation of the acceleration curve is relatively large during the commutation process. This may be interpreted as follows:

1. When the nonlinear perturbation mathematical model is established, the mechanical clearance is not compensated, because it is relatively small. However, for the high following frequencies, the presence of clearance gives the following error curve a large spike.
2. Due to the limitations of the encoder resolution at low speeds, the feedback position signal is seriously quantified, resulting in the fluctuation of control signal and additional tracking error.
3. The mismatch phenomenon exists in the controlled object model so that the composite 2-DOF IMC controller cannot fully perform the control characteristics. Moreover, the controller parameters should be optimized.

## 7. Conclusion

This paper presents a composite 2-DOF IMC controller for a new ARR, which focuses on a specific control strategy. The specific function of the new ARR and examples involving the passive follow function, active control trajectory follow function and impedance training function are presented in this paper. The PID controller and the compound 2-DOF IMC controller are designed for position control. It was demonstrated that the composite 2-DOF IMC controller significantly outperformed the PID controller in terms of the control effect. The effectiveness of passive training of the given trajectory and the impedance training active control strategy was proven by the human-machine experiment. The obtained results show that the designed control system enabled a safe, stable and reliable operation of the robot with a small following error.

## References

1. G. S. Sawicki and D. P. Ferris, "A pneumatically powered knee-ankle-foot orthosis (KAFO) with myoelectric activation and inhibition," *J. NeuroEng. Rehabil.* **6**(1), 1–16 (2009).
2. R. Lu, Z. Li, C. Su and A. Xue, "Development and learning control of a human limb with a rehabilitation exoskeleton," *IEEE Trans. Ind. Electron.* **61**(7), 3776–3785 (2014).
3. D. W. Alexander, J. V. Zitzewitz, A. Caprez, L. Lunenburger and R. Riener, "Path control: A method for patient-cooperative robot aided gait rehabilitation," *IEEE Trans. Neural Syst. Rehabil. Eng.* **18**(1), 38–48 (2010).
4. J. Deutsch, J. Latonio, G. Burdea and R. Boian, "Post-stroke rehabilitation with the Rutgers ankle system: A case study," *Presence-Teleoper. Virtual Environ.* **10**(4), 416–430 (2001).
5. R. F. Boian, M. Bouzit, G. C. Burdea, J. Lewis and J. E. Deutsch, "Dual Stewart Platform Mobility Simulator," *Proceedings of the 2005 IEEE 9th International Conference on Rehabilitation Robotics*, Chicago, IL, USA (2005) pp. 550–555.
6. R. Riener, L. Lünenburger and G. Colombo, "Human-centered robotics applied to gait training and assessment," *J. Rehabil. Res. Dev.* **43**(5), 679–694 (2006).
7. M. Zhang, S. Q. Xie, X. Li, G. Zhu, W. Meng, X. Huang and J. V. Allan, "Adaptive patient-cooperative control of a compliant ankle rehabilitation robot (CARR) with enhanced training safety," *IEEE Trans. Ind. Electron.* **65**(2), 1398–1407 (2018).
8. S. Q. Xie and P. K. Jamwal, "An iterative fuzzy controller for pneumatic muscle driven rehabilitation robot," *Expert Syst. Appl.* **38**(7), 8128–8137 (2011).
9. A. Roy, H. I. Krebs, S. L. Patterson, T. N. Judkins, I. Khanna, L. W. Forrester, R. M. Macko and N. Hogan, "Measurement of Human Ankle Stiffness using the Anklebot," *Proceedings of the 2007 IEEE 10th International Conference on Rehabilitation Robotics*, Noordwijk, The Netherlands (2007) pp. 356–363.
10. A. Roy, H. I. Krebs, D. J. Williams, C. T. Bever, L. W. Forrester, R. M. Maeko and N. Hogan, "Robot-aided neuro rehabilitation: A novel robot for ankle rehabilitation," *IEEE Trans. Robot.* **25**(3), 569–582 (2009).
11. J. Stein, H. I. Krebs, W. R. Frontera, S. E. Fasoli, R. Hughes and N. Hogan, "Comparison of two techniques of robot-aided upper limb exercise training after stroke," *Am. J. Phys. Med. Rehabil.* **83**(9), 720–728 (2004).

https://doi.org/10.1017/S0263574719001188 Published online by Cambridge University Press

12. H. Azcaray, A. Blanco, C. García, M. Adam, J. Reyes, G. Guerrero and C. Guzmán, "Robust GPI control of a new parallel rehabilitation robot of lower," *Int. J. Control Autom. Syst.* **16**(5), 2384–2392 (2018).
13. S. Bachir and C. Duvanaud, "Linearization of radio frequency amplifiers using nonlinear Internal Model Control method," *AEU-Int. J. Electron. Commun.* **65**(6), 495–501 (2011).
14. S. Wen, B. Zhang, P. Hao, H. K. Lam and H. Wang, "Fuzzy fractional order force control of 6PUS-UPU redundantly actuated parallel robot based on inner model position control structure," *Eng. Appl. Artif. Intell.* **65**, 200–211 (2017).
15. C. Zhou and N. Sagarakis, "On the comprehensive kinematics analysis of a humanoid parallel ankle mechanism," *J. Mech. Robot.* **10**(5), 051015 (2018).
16. M. F. Eilenberg, H. Geyer and H. Herr, "Control of a powered ankle-foot prosthesis based on a neuromuscular model," *IEEE Trans. Neural Syst. Rehabil. Eng.* **18**(2), 164–173 (2010).
17. Y. L. Park, B. R. Chen, O. N. Pérez-Arancibia, D. Young, L. Stirling, R. J. Wood, E. C. Goldfield and R. Nagpal, "Design and control of a bio-inspired soft wearable robotic device for ankle–foot rehabilitation," *Bioinspir. Biomim.* **16**(5), 200–211 (2017).
18. J. S. Dai, T. Zhao and C. Nester, "Sprained ankle physiotherapy based mechanism synthesis and stiffness analysis of a robotic rehabilitation device," *Auton. Robot.* **16**(2), 207–218 (2004).
19. P. K. Jamwal, S. Hussain and S. Q. Xie, "Three-stage design analysis and multicriteria optimization of a parallel ankle rehabilitation robot using genetic algorithm," *IEEE Trans. Autom. Sci. Eng.* **12**(4), 1433–1446 (2015).
20. P. K. Jamwal, S. Q. Xie, S. Hussain and J. G. Parsons, "An adaptive wearable parallel robot for ankle injury treatments," *IEEE-ASME Trans. Mechatron.* **19**(1), 64–75 (2014).
21. L. Wang, H. Zhu and Z. Chen, "Modeling and Control of Ankle Rehabilitation Robot with Nonlinear Factors," *Proceeding of the IEEE International Conference on Information and Automation*, Hailar, China (2014) pp. 64–75.
22. Z. Li, D. Fan and S. Fan, "Lugre-model-based friction compensation in direct-drive inertially stabilized platforms," *6th IFAC Symp. Mechatron. Syst.* **46**(5), 636–642 (2013).
23. M. R. Sobczyk, V. I. Gervini, E. A. Perondi and M. A. B. Cunha, "A continuous version of the Lugre friction model applied to the adaptive control of a pneumatic servo system," *J. Frankl. Inst.-Eng. Appl. Math.* **353**(13), 3021–3039 (2016).
24. L. Lu, B. Yao, Q. Wang and Z. Chen, "Adaptive robust control of linear motors with dynamic friction compensation using modified LuGre model," *Automatica* **45**(12), 2890–2896 (2009).
25. K. Johanastrom and C. Canudas-de-Wit, "Revisiting the LuGre friction model," *IEEE Control Syst. Mag.* **28**(6), 101–114 (2008).
26. C. C. De Wit, H. Olsson, K. J. Astrom and P. Lischinsky, "A new model for control of systems with friction," *IEEE Trans. Autom. Control* **40**(3), 419–425 (1995).
27. Y. Xiong and Y. Li, "Modified internal model control scheme for the drive part with elastic joints in robotic system," *J. Intell. Robot. Syst.* **79**(3–4), 475–485 (2015).
28. Q. Li, A. N. Poo and C. M. Lim, "Internal model based fault tolerant control of a robot manipulator," *Mechatronics* **6**(5), 571–590 (1996).
29. Q. Wang, Q. Bi and Y. Zhang, "Partial internal model control," *IEEE Trans. Ind. Electron.* **48**(5), 976–982 (2001).
30. P. Cui, D. Zhang, S. Yang and H. Li, "Friction compensation based on time delay control and internal model control for gimbal system in MSCMG," *IEEE Trans. Ind. Electron.* **64**(5), 3798–3807 (2016).
31. Q. Zhu, Z. Yin, Y. Zhang, J. Niu, Y. Li and Y. Zhong, "Research on two-degree-of-freedom internal model control strategy for induction motor based on immune algorithm," *IEEE Trans. Ind. Electron.* **63**(3), 1981–1992 (2016).
32. D. Camposgaona, R. Penaalzola, J. L. Monroymorales, M. Ordonez, O. Anayalara and W. Leithead, "Fast selective harmonic mitigation in multifunctional inverters using internal model controllers and synchronous reference frames," *IEEE Trans. Ind. Electron.* **64**(8), 6338–6349 (2017).

https://doi.org/10.1017/S0263574719001188 Published online by Cambridge University Press